Research Square

Preprints are preliminary reports that have not undergone peer review.
They should not be considered conclusive, used to inform clinical practice,
or referenced by the media as validated information.

Al2O3 barrier-controlled sign reversal and giant enhancement of third-order optical nonlinearity in Ag/AuNP-Al2O3-PdO nanocomposite films under femtosecond excitation.

Valentyn Rudenko

val@iop.kiev.ua

Institute of Physics

Viktor Styopkin

Institute of Physics

Volodymyr Liakhovetskyi

National Technical University of Ukraine “Igor Sikorsky Kyiv Polytechnic Institute”

Research Article

Keywords: nonlinear optics, Z-scan, χ (3) , plasmonics, nanoparticle-on-mirror, hot-electron tunneling, PdO, saturable absorption

Posted Date: October 8th, 2026

DOI: https://doi.org/10.21203/rs.3.rs-11142252/v1

License: This work is licensed under a Creative Commons Attribution 4.0 International License.
Read Full License

Additional Declarations: No competing interests reported.

Al_2O_3 barrier-controlled sign reversal and giant enhancement of third-order optical nonlinearity in Ag/AuNP-Al_2O_3-PdO nanocomposite films under femtosecond excitation.

Valentyn Rudenko(ORCIDID: 0000-0002-5500-6026)[a*], Viktor Styopkin(ORCIDID: 0000-0003-0199-146X)[a], Volodymyr Liakhovetskyi(ORCIDID: 0000-0002-0419-5779)[a,b],

[a]*Institute of Physics of the National Academy of Sciences of Ukraine, Kyiv, Ukraine*
[b]*National Technical University of Ukraine "Igor Sikorsky Kyiv Polytechnic Institute", 37, Peremohy Avenue, Kyiv 03056, Ukraine*
** Corresponding author: Valentyn Rudenko (val@iop.kiev.ua, valentyn.rudenko@outlook.com)*

Abstract

Engineering the sign and magnitude of the complex third-order nonlinear susceptibility $\chi^{(3)}$ in plasmonic nanocomposites remains a central challenge for the design of ultrafast optical limiters, nonlinear phase elements, and saturable absorbers. We report femtosecond Z-scan characterization (λ = 800 and 400 nm, τ_p = 176 fs) of Ag/AuNP-Al_2O_3-PdO nanocomposite films with Al_2O_3 spacer thickness varied from 1.5 to 12 nm. The sign of nonlinear refractive index n_2 at 800 nm switches systematically from negative (1.5 nm, hot-electron tunneling) to positive (6 nm, electronic Kerr) to negative (12 nm, Au interband contribution), providing the first experimental demonstration of sign-programmable $\chi^{(3)}$ through dielectric spacer engineering in a single material system. A 16-nm PdO overlayer on the 6-nm spacer sample enhances $|\chi^{(3)}|$ by a factor of 1625, reaching 2.52×10^{-8} esu via nanoparticle-on-mirror gap-plasmon resonance. PdO induces n_2 sign reversal in the 12-nm sample through Pd^{2+} *d*-electron Kerr nonlinearity. At 400 nm, the core-shell sample exhibits a reversible SA→RSA→SA transition attributable to sequential saturation of two localized surface plasmon resonance modes. These results define nanometer-scale design rules for $\chi^{(3)}$ engineering in Ag/Au nanocomposite films.

Keywords: nonlinear optics, Z-scan, $\chi^{(3)}$, plasmonics, nanoparticle-on-mirror, hot-electron tunneling, PdO, saturable absorption

1. Introduction

The third-order optical nonlinearity of noble metal nanoparticles (NPs) has remained an active area of research for several decades. This is due to the unique ability of localized surface plasmon resonance (LSPR) to concentrate electromagnetic energy at the nanoscale and, thus, to enhance the nonlinear optical response by several orders of magnitude compared to bulk materials [1, 2]. The third-order nonlinear optical susceptibility $\chi^{(3)}$ governs a broad class of technologically significant phenomena: nonlinear refraction, two-photon absorption, saturated and reverse-saturated absorption. Furthermore, its sign and magnitude determine whether the material acts as a self-focusing or self-defocusing medium, a passive optical limiter, or an ultrafast all-optical switch [3, 4]. The independent control of both the sign and the magnitude of $Re\chi^{(3)}$, and achieving this through structural design rather than merely wavelength tuning, remains one of the major unsolved problems in nanophotonic materials engineering.

Among plasmonic systems, Ag/Au bimetallic nanostructures occupy a special place: silver provides the highest enhancement of the plasmonic field in the visible range, while gold provides chemical stability and a strong interband absorption edge near 500 nm, which significantly alters the nonlinear dynamics under near-resonant excitation [5]. The nonlinear refractive index n_2 of Ag

and Au nanoparticles in transparent matrices arises primarily due to the in-band Kerr effect of quasi-free electrons, which yields a negative value of $Re\chi^{(3)}$ for isolated spherical particles [6, 7]. However, the sign of $Re\chi^{(3)}$ can vary depending on the local dielectric medium, particle geometry, and the balance between electronic and thermal contributions under different pulsed regimes [8]. In our previous work on Ag/Au nanocomposite films coated with Al_2O_3 dielectric layers of varying thicknesses, we demonstrated that nanoscale structuring of the dielectric shell (without changing the composition of the substrate) is sufficient to control not only the magnitude but also the sign of $\chi^{(3)}$ in femtosecond and nanosecond excitation modes in the 400-1064 nm range [9]. It was shown there that the nonlinear response at 800 nm under femtosecond excitation was exclusively electronic, with maximum values of n_2 and β observed at 400 nm due to a combination of near-resonant LSPR enhancement and interband excitation in gold. At the same time, the observed change in the sign of n_2 with increasing Al_2O_3 thickness was due to competition between hot carrier tunneling and the Kerr electronic mechanism.

A logical extension and the objective of this work is to introduce a second functional material on top of the Al_2O_3 layer: palladium oxide (PdO). This choice is based on three independent considerations. First, PdO is a semiconductor with a direct bandgap $E_g \approx 1.7$-2.8 eV [10], which has an optical absorption edge in the visible range and provides an unambiguous, sub-band contribution of bound electrons to $Re\chi^{(3)}$ at 800 nm ($1.55\ \text{eV} < E_g$) via virtual transitions [11]. Second, we have previously demonstrated that PdO thin films inherently exhibit high third-order optical nonlinearity under nanosecond excitation, with $|\chi^{(3)}|$ reaching values competitive with Au nanocomposites [12]. Third, our previous structural study of AuNP-Al_2O_3-PdO trilayers established that the thickness of the Al_2O_3 barrier controls LSPR attenuation and influences charge transfer between gold nanoparticles and PdO. Moreover, the position and width of the plasmon resonance are sensitive to the Al_2O_3 thickness [13]. Further Z-scan measurements of AuNP-Al_2O_3-PdO under nanosecond excitation at wavelengths of 1064 and 532 nm confirmed that the sign of the nonlinear refraction also depends on the illumination geometry in such heterostructures [14].

It is important to emphasize that this system differs significantly from previous studies based on AuNPs, since replacing pure gold nanoparticles with Ag/Au bimetallic nanoparticles creates a double LSPR structure, as evidenced by two distinct resonance peaks at 409-414 nm and 513-517 nm for samples S1 and S2, which are absent in AuNP systems. Moreover, the short-wavelength component at 409-414 nm can directly resonate with the 400 nm excitation used, providing a channel for plasmon field amplification that does not exist in heterostructures with pure gold nanoparticles. This spectral feature, combined with the special role of Ag in the in-band Kerr mechanism, radically alters the nonlinear optical properties even before the addition of the PdO layer.

The key parameter determining the structure of the samples under study is the thickness of the Al_2O_3 layer: $d(Al_2O_3) = 1.5$, 6, and 12 nm. In the quantum mechanical tunneling model, the probability of hot carrier transport from Ag/Au nanoparticles through Al_2O_3 into PdO is proportional to $exp(-2kd)$, where $k \sim 5$-$8\ \text{nm}^{-1}$ for amorphous Al_2O_3 [15]. This implies that $d(Al_2O_3) = 1.5$ nm (nearly transparent barrier) and $d(Al_2O_3) = 12$ nm (strongly confined tunneling) represent two qualitatively distinct modes of Ag-PdO interaction. Meanwhile, $d(Al_2O_3) = 6$ nm is an intermediate point between potentially competing mechanisms. Each sample has one half covered with PdO and one half without PdO, identical in NP geometry and Al_2O_3 thickness, which allows us to isolate the contribution of PdO under otherwise identical illumination conditions - this is an internal control that is lacking in most published studies of heterostructures.

Despite the extensive literature on metal nanoparticles in oxide matrices [4] and PdO as a standalone nonlinear material [12], no study has addressed the following question: Is it possible to

change the sign of $Re\chi^{(3)}$ in a three-component metal/ultra-thin oxide/semiconductor oxide heterostructure by varying the thickness of the intermediate barrier at a fixed excitation wavelength and pulse duration? This question is non-trivial, since the resulting $Re\chi^{(3)}$ is a superposition of at least three components: the in-band Kerr electronic mechanism of Ag/Au nanoparticles, the bound electron mechanism of PdO in the sub-gap region, and the local field enhancement factor $\chi^{(3)} \propto |f_{loc}|^4$ [1] - each of which depends differently on d(Al_2O_3). At the same time, it is expected that the absorption nonlinearity ($Im\chi^{(3)}$) will reflect the competition between saturating absorption via LSPR bleaching and reverse saturating absorption via transitions to the excited state [16, 17]. In this case, the balance is determined by whether hot carriers are confined within the Ag/Au nanoparticles (thick Al_2O_3 barrier) or are rapidly transported to the PdO trap states (thin Al_2O_3 barrier).

In this article, we report the results of comprehensive femtosecond Z-scan measurements (τ_p = 176 fs, λ = 800 and 400 nm) of Ag/Au-Al_2O_3-PdO heterostructures with three different Al_2O_3 layer thicknesses, combined with spectral analysis of six sample configurations. We demonstrate: (i) a PdO-induced sign change of n_2 at 800 nm for the sample with a thick Al_2O_3 barrier (d = 12 nm), arising from the dominance of the PdO contribution to $Re\chi^{(3)}$ in the sub-gap region, where electronic coupling with the low-energy band is suppressed; (ii) a three-order-of-magnitude enhancement of $|\chi^{(3)}|$ caused by nonlinear absorption of PdO; (iii) the manifestation of reverse saturable absorption in the sample with a thick barrier at 400 nm, which is explained by the trapping of hot carriers, ensuring effective filling of the excited state; and (iv) threshold two-step saturation dynamics in a sample with an intermediate Al_2O_3 barrier (d = 6 nm), indicating sequential saturation of interphase trap states and bulk absorption of PdO. These results confirm that the engineering of Al_2O_3 barriers is a promising design approach for simultaneously controlling the sign, magnitude of $\chi^{(3)}$, and mechanism of nonlinear absorption in a single plasmonic heterostructure.

2. Materials and Methods

2.1 Sample preparation

Three-component heterostructures of the Ag/AuNP-Al_2O_3-PdO type were fabricated by sequential deposition on optical-grade glass substrates. Prior to use, the substrates were surface-treated in a "Piranha" solution (H_2SO_4: H_2O_2 = 3:1) at 70 °C for 60 minutes, after which they were rinsed with distilled water and dried under laboratory conditions.

The plasmonic core was formed from a two-layer metal precursor - first, a 7-nm layer of silver (Ag) was deposited, which was immediately covered with a 0.7-nm layer of gold (Au); both layers were deposited by resistive thermal evaporation at a residual pressure of (3-5)×10^{-6} Torr, with the thickness continuously monitored using quartz crystal microbalances. Under a controlled annealing cycle in a programmable furnace, the continuous film turns into a nanoparticle ensemble. The sample was placed in the furnace at 400 °C, heated at a rate of 60 °C/min to 680 °C under a partial vacuum of 30 Torr, held at the peak temperature for 2 min, and then cooled at a rate of 40-50 °C/min. At 450 °C, air was let in, and the furnace chamber was opened to laboratory air. Atmospheric air was introduced at a temperature of 450 °C. The substrates were removed at 400 °C and left to cool on a laboratory bench. To prevent the influence of air moisture, all samples were stored in a sealed desiccator filled with silica gel. Particle morphology was determined using a scanning electron microscope (JEOL JSM-35). The resulting size distribution covers the range of 25-120 nm, with an average diameter of about 60 nm and a standard deviation of 13 nm, which corresponds to our group's previous data on this preparation method [9, 13].

The Al_2O_3 dielectric barrier was formed through iterative cycles of resistive evaporation of metallic Al at a pressure of (3-5)×10^{-6} Torr, with each sublayer having a thickness of 1.0-1.5 nm, and a

natural oxidation step in open air was performed between successive cycles. The oxide thickness $t(Al_2O_3)$ was derived from the deposited Al thickness $t(Al)$ via the stoichiometric expansion ratio established in Ref. [14]:

$$\frac{t(Al_2O_3)}{t(Al)} = 1.38 \pm 0.04 \quad (1)$$

Three barrier thickness options were selected: 1.5 nm (sample S1), 6 nm (sample S2), and 12 nm (sample S3).

The outermost PdO layer was formed by depositing a Pd metal film and subsequent Pd oxidation. Pd film was deposited via evaporation at a pressure of (3-5)×10^{-6} Torr to a nominal thickness calculated so that 16 nm of oxide would form after conversion. The film was then oxidized at a temperature of 500-550 °C for 30 min in a static air atmosphere. The relationship between the deposited Pd thickness $t(Pd)$ and the resulting PdO thickness $t(PdO)$ follows the empirical ratio given in Ref. [14]:

$$\frac{t(PdO)}{t(Pd)} = 1.68 \quad (2)$$

Prior to PdO deposition, a mechanical mask was applied to one half of each substrate, leaving that area uncoated. This one-step masking approach creates a pair of six configurations: S1, S2, S3 (reference halves, without PdO) and S1+PdO, S2+PdO, S3+PdO, in which the NP morphology, Al_2O_3 thickness, and substrate are strictly identical within each pair, providing built-in differential control to isolate the PdO contribution. The total effective film thicknesses, determined based on deposition calibration and confirmed by transmission analysis, are L = 9.2, 13.7, and 19.7 nm for the reference series and L = 25.2, 29.7, and 35.7 nm for the PdO series, respectively.

2.2 Structural and Linear Optical Characterization

The obtained Ag/AuNPs were studied using a JSM-35 (JEOL) scanning electron microscope (SEM).

Transmission spectra for all six configurations were obtained in the range from 300 to 900 nm using a Shimadzu UV-2450 double-beam spectrophotometer, with a clean glass substrate serving as the reference sample. The wavelength-resolved linear absorption coefficient $\alpha_0(\lambda)$ was obtained using the single-pass Beer-Lambert law $T(\lambda) = exp(-\alpha_0(\lambda)L)$; the values obtained at λ = 400 and 800 nm for each configuration are shown in Table 1.

A methodologically important point concerns the PdO-coated samples: their combined α_0 values at both probe wavelengths differ significantly from those of the uncoated reference halves: by a factor of 2.5-3.5 at 800 nm (for example, α_0 increases from 2.45×10^4 to 8.69×10^4 cm^{-1} for S1 after PdO deposition) and by a factor of 3-7 at 400 nm. Accordingly, the effective interaction length $L_{eff} = [1-exp(-\alpha_0 L)]/\alpha_0$ was calculated separately for each of the six configurations at each wavelength, always using the total α_0 of the corresponding structure. Failure to apply this correction for each configuration would have led to a systematic overestimation of $|\chi^{(3)}|$ in the PdO series, which was explicitly avoided in this work.

2.3 Z-scan Measurements

Third-order nonlinear optical coefficients were measured using a single-beam Z-scan method [3] using a femtosecond amplification system based on Ti: sapphire (Coherent Mira-900F generator + Legend HE regenerative amplifier), which generates pulses with a duration of 176 fs and a

repetition rate of 1 kHz. The fundamental output signal at 800 nm and its second harmonic at 400 nm (generated in a β-BBO crystal with the residual fundamental frequency rejected by a dichroic separator) were used in independent measurement sessions.

Simultaneous two-channel geometry was employed in each measurement. An open-aperture (OA) channel, which collects the total transmitted power in the far field, was used to determine the nonlinear absorption coefficient β and the saturation intensity I_s. The closed-aperture (CA) channel, with a far-field aperture having a linear transmittance $S \approx 0.47$ at 800 nm and $S \approx 0.22$ at 400 nm, was used to determine the nonlinear refractive index n_2. The peak intensity I_0 at the beam waist was established by rotating a half-wave plate in front of the Glan-Taylor polarizer and calibrated using the measured focal spot radius w_0. The Rayleigh range $z_R = \pi w_0^2/\lambda$ exceeded the sample thickness by at least two orders of magnitude in all cases, confirming the validity of the approximation for thin samples.

At 800 nm, a single intensity value of $I_0 \approx$ 10-12 GW/cm^2 was used for all six configurations, sufficient to characterize the nonlinear response, which is practically independent of intensity in this off-resonance region of the spectrum. At 400 nm, where both n_2 and β both exhibit a pronounced dependence on intensity, measurements for each PdO-coated sample were repeated at five to six discrete values of I_0 in the range of 4.71-31.43 W/cm^2, which allowed for a systematic characterization of the saturation dynamics and RSA described in Section 3.

2.4 Data analysis and extraction of $\chi^{(3)}$

Closed-aperture traces were fitted to the analytical transmittance expression of Kwak et al. [18]:

$$T_{CA}(z) = \frac{1}{1+\frac{4x}{(x^2+1)^2}\Delta\Phi_0+\frac{4}{(x^2+1)^3}\Delta\Phi_0^2}, \quad (3)$$

where $x=z/z_0$ is the normalized sample position, z_0 the Rayleigh length, and $\Delta\Phi_0 = (2\pi/\lambda)n_2 I_0 L_{eff}$ the on-axis nonlinear phase shift. This expression accounts simultaneously for nonlinear refraction and absorption and remains accurate for $|\Delta\Phi_0|$ up to π, which encompasses all phase shifts encountered in the present samples.

The OA Z-scan data were approximated using a two-mechanism model proposed by Zhang et al. [19], which accounts for the coexistence of saturated absorption (SA) and reverse-saturated absorption (RSA):

$$T_{OA}(z) = \left(1 - \frac{\beta I_0 L_{eff}}{2\sqrt{2}(1+x^2)}\right)\left(1 + \frac{I_0}{I_s(1+x^2)}\right), \quad (4)$$

An analysis of OA Z-scan data at a laser wavelength of 400 nm revealed a systematic discrepancy between the approximation curve profile according to Equation 4 and the obtained data. It was therefore hypothesized that, in this case, the non-linear absorption process is of a higher order in terms of intensity and exhibits the characteristics of competing channels (SA+RSA/2PA). Therefore, to fit the OA data at a wavelength of 400 nm, the formula by Sheik-Bahae [3] was used and expanded to the second term of the series:

$$T_{OA}(z) = \sum_m \frac{[-q_0(z)]^m}{(m+1)^{3/2}} = 1 - \frac{q}{2\sqrt{2}(1+x^2)} + \frac{q^2}{3\sqrt{3}(1+x^2)^2} - \cdots, \quad (5)$$

where $q_0 = \beta L_{eff} I_0$ (the standard 2PA parameter). This significantly improved the quality of the fitting, thereby confirming the presence of yet another competing absorption channel.

The third-order complex sensitivity $\chi^{(3)}$ was calculated from the determined n_2 and β using [9, 14]:

$$Re\chi^{(3)}[esu] = \frac{n_0^2 \varepsilon_0 c^2}{10^4 \pi} n_2 \left[\frac{cm^2}{W}\right], \quad (6)$$

$$Im\chi^{(3)}[esu] = \frac{n_0^2 \lambda \varepsilon_0 c^2}{4\pi^2 10^2} \beta \left[\frac{cm}{W}\right], \quad (7)$$

$$\left|\chi^{(3)}\right| = \sqrt{(Re\chi^{(3)})^2 + (Im\chi^{(3)})^2} \quad (8)$$

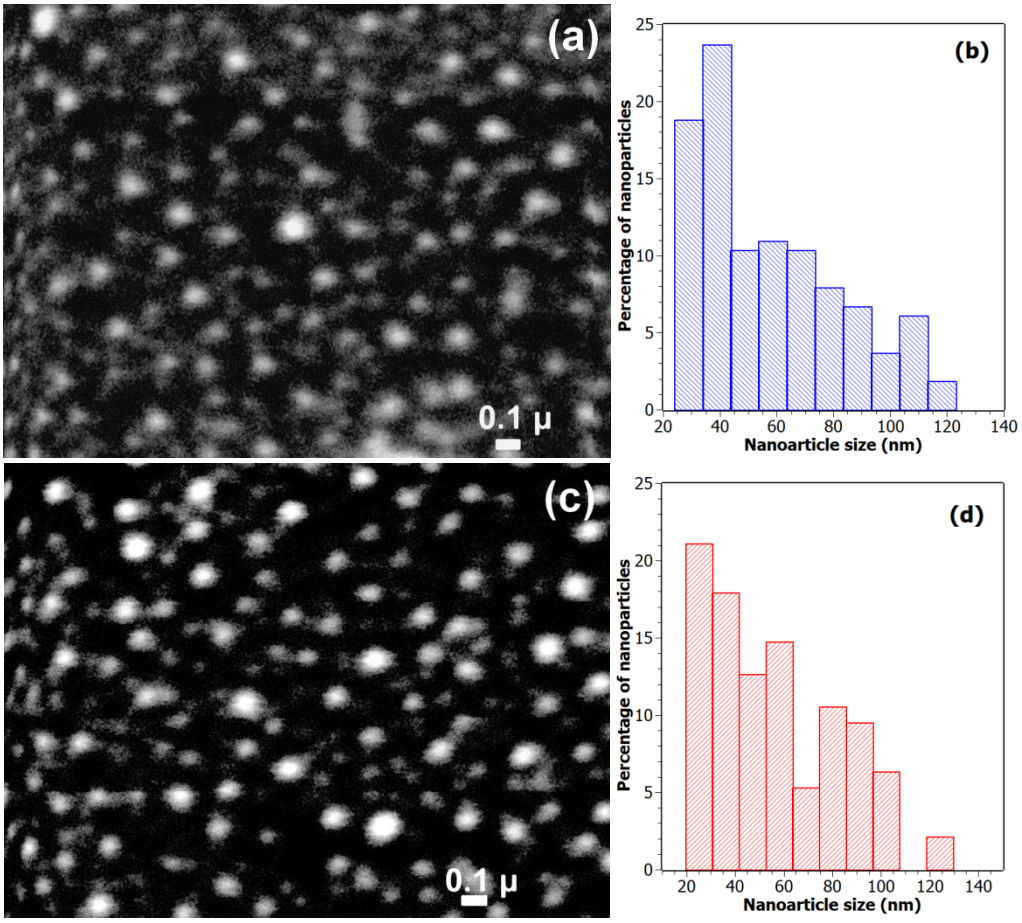
where n_0 is the linear refractive index of the composite film, ε_0 is the permittivity of free space, c is the speed of light in a vacuum, and λ is the excitation wavelength. All $\chi^{(3)}$ values are quoted in Gaussian *esu* units throughout, in keeping with the convention adopted in the literature on metal nanoparticle composites [4]. Each Z-scan measurement was repeated at least three times; the values given represent the average, and the standard deviations are within 10% for n_2 and 15% for β.

3. Results

3.1. Linear optical spectra and structural parameters

Figures 1a, 1c and 1e show scanning electron microscope (SEM) images of the nanoparticles (NPs) in samples S1, S2 and S3, respectively. A comparison of the images shows that the distribution of NPs in all the samples is similar. The distributions of NP sizes in samples S1, S2 and S3 are presented in Figures 1b, 1d and 1f, respectively. These confirm the similarity of the NPs in the samples. The majority of the NPs are between 30 and 120 nm in size. The average NP size is around 60-70 nm, with a standard deviation of 15 nm.

Thus, deposition of Al_2O_3 does not sufficiently influence the NPs. The Al_2O_3 layers are thin, and Al does not significantly heat the substrate during deposition (the melting point of Al is rather low). Al_2O_3 provides stability to the distribution of NPs for different thicknesses of its layer.



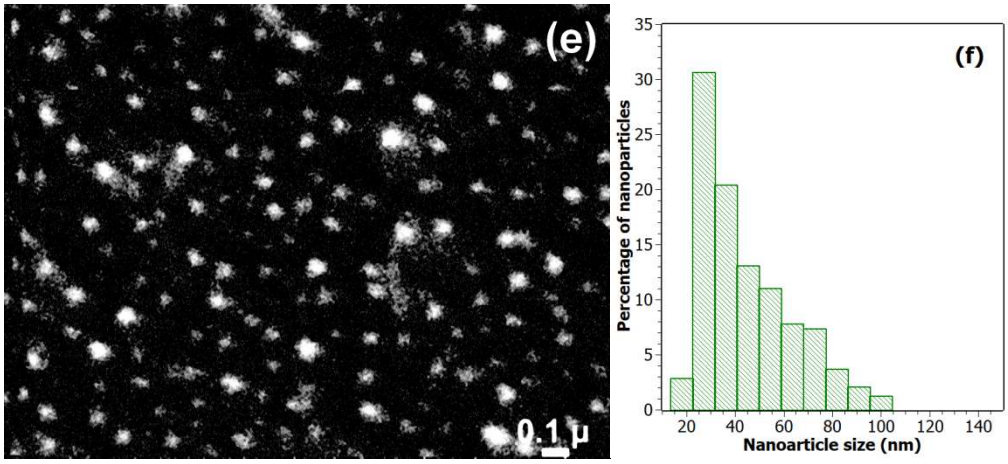


Fig. 1 SEM images (a, c, e) and size distributions (b, d, f) of Ag/Au nanoparticles in multilayer structures S1-S3

The structural and linear optical parameters of all six sample configurations studied are presented in Table 1. Figure 1 shows the extinction spectra for the complete set of samples in the 300-900 nm range. The spectra of the sample configurations without a PdO layer (S1, S2, S3) are shown as solid lines, while the spectra for the configurations with a PdO layer (S1+PdO, S2+PdO, S3+PdO) are shown as dashed lines. The vertical dashed lines indicate the two Z-scan excitation wavelengths (400 and 800 nm).

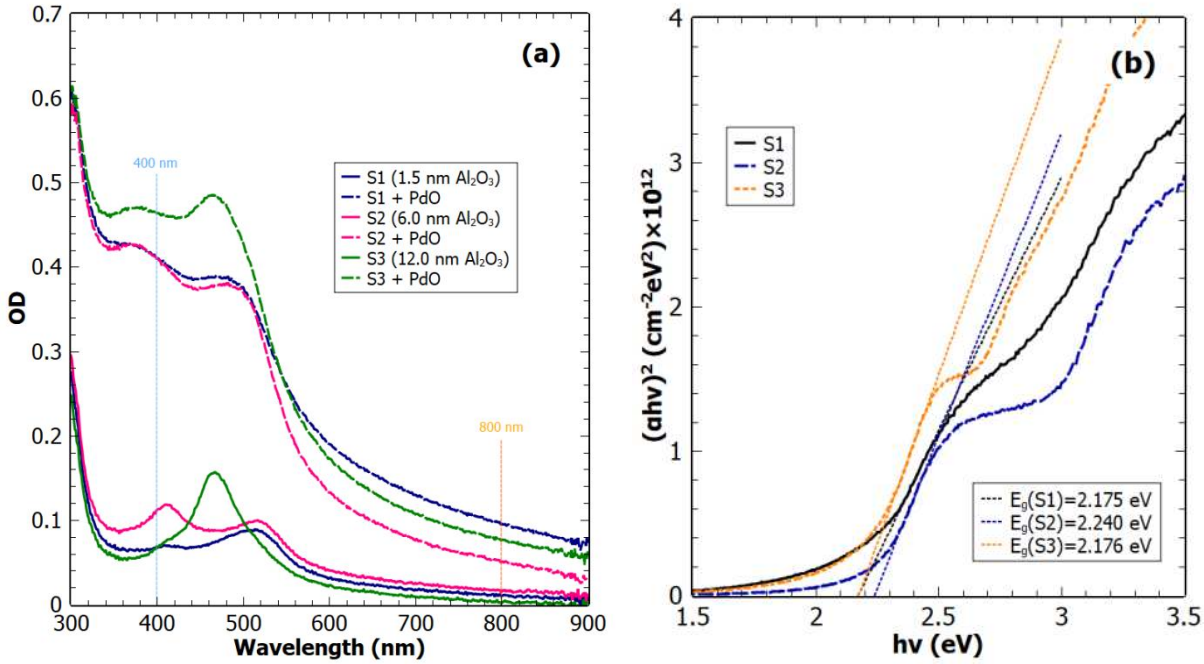


Fig. 2 (a) Optical density spectra of Ag/AuNP-Al_2O_3 (solid lines) and Ag/AuNP-Al_2O_3-PdO (dashed lines) structures with Al_2O_3 thicknesses of 1.5 nm (S1), 6 nm (S2), and 12 nm (S3). Vertical dotted lines mark the Z-scan excitation wavelengths (400 and 800 nm). (b) Tauc plots *[(αhv)^2* vs. hv] for the corresponding PdO-containing configurations; dashed lines indicate linear extrapolations for bandgap (E_g) determination. Extracted E_g values: 2.175 eV (S1+PdO), 2.240 eV (S2+PdO), and 2.176 eV (S3+PdO)

The morphology of the Ag/Au nanoparticle layers without a PdO coating, as determined by scanning electron microscopy (SEM), along with the corresponding particle size distribution, is shown in Fig. 1. The SEM images confirm that the synthesis method used allows for the production of well-separated Ag/Au nanoisland particles with diameters in the range of 30-120 nm and an average diameter of approximately 60-70 nm (standard deviation ~13 nm), which is fully consistent

with the data for this fabrication method presented in [9]. Importantly, the size distribution of the nanoparticles and their surface density do not change systematically with respect to the Al_2O_3 thickness in the three samples, indicating that the dielectric top layer does not cause significant coalescence or redistribution of the particles under the deposition conditions used. This morphological homogeneity is a necessary condition for attributing the differences in the nonlinear optical response between S1, S2, and S3 to the barrier thickness d(Al_2O_3) rather than to changes in the plasmonic core.

The extinction spectra of samples S1, S2, and S3 (Fig. 2a, solid lines) demonstrate a clear dependence of the LSPR profile on the Al_2O_3 thickness, even though the nanoparticles in all three samples are morphologically close. This dependence reflects the sensitivity of the plasmon resonance to the effective dielectric permittivity ε_{eff} of the surrounding medium (Al_2O_3). It increases with the thickness of Al_2O_3, since the oxide shell occupies an increasingly larger fraction of the volume in the near field around each nanoparticle.

Samples S1 and S2 exhibit a two-peaked extinction curve. Two distinct maxima in optical density are observed at 409 and 513 nm for S1 and at 414 and 517 nm for S2. Incomplete doping preserves a certain degree of compositional heterogeneity between domains dominated by silver or gold. In this case, the short-wavelength component (409-414 nm) corresponds to the dipole plasmon mode of silver-rich zones in bimetallic nanoparticles. The long-wavelength component (513-517 nm), in turn, reflects the plasmonic properties associated with Au-rich domains and the collective response of the partially alloyed Ag/Au system [9]. The coexistence of these two spectral features is interpreted as evidence of incomplete mixing of Ag and Au within the nanoparticles under the applied annealing conditions, rather than the formation of a homogeneous alloy. This two-peak structure is preserved in both S1 and S2, since a thin (1.5 nm) or medium (6 nm) Al_2O_3 barrier maintains sufficient electromagnetic contrast between the nanoparticle and its surroundings to sustain two spectrally separated resonance branches.

In S3 (d = 12 nm), the two-peak structure merges into a single, broader extinction maximum at 466 nm. We attribute this behavior to the formation of a silver-gold alloy. It is known that such a structure can exhibit precisely these plasmonic properties [9]. The position of this merged resonance at 466 nm is shifted toward the long-wavelength side by 52-57 nm relative to the short-wavelength LSPR peaks S1 and S2, which corresponds to the expected "red" shift of the plasmon resonance upon an increase in the dielectric loading. The highest optical density at the LSPR peak for configurations without a PdO coating, OD_{max} = 0.157 at 466 nm, is observed in sample S3. This indicates the highest effective strength of the merged resonance oscillator under conditions of strong dielectric confinement.

In terms of the excitation wavelength during Z-scanning (Fig. 1, dotted lines), the short-wavelength LSPR components S1 (409 nm) and S2 (414 nm) are close to resonance with the 400 nm laser wavelength used, providing a resonant channel for local field enhancement. This is not the case for S3, whose combined LSPR resonance peak at 466 nm is spectrally shifted by ~ 66 nm relative to the 400 nm laser excitation wavelength. At the 800 nm wavelength, all three LSPR profiles decay to values close to the baseline. This confirms that the 800 nm laser excitation operates in the transparency window outside the resonance for all uncoated samples.

The optical bandgap width E_g of the PdO layer for the sample configuration with a deposited PdO layer was determined based on an analysis of the Tauc plot. In this case, the standard relationship for direct-bandgap semiconductors was used: $(\alpha h\nu)^2 \propto (h\nu - E_g)$. The resulting plots are shown in Fig. 1b. The determined values are E_g = 2.175 eV (S1+PdO), 2.240 eV (S2+PdO), and 2.176 eV (S3+PdO), corresponding to absorption edge wavelengths λ_g = 570, 553, and 570 nm,

respectively. These values fall within the range of E_g = 1.7-2.8 eV reported in the literature for thin PdO films with different stoichiometry's and microstructures [10].

The difference in E_g among the three configurations (with S2+PdO exhibiting a significantly wider bandgap) may indicate a change in the electronic structure of PdO caused by the degree of interaction with the Ag/Au nanoparticle layer through the Al_2O_3 barrier. Since the PdO layer is deposited under identical conditions in all cases, relative changes in E_g may occur due to changes in charge transfer interactions between the metal nanoparticles and PdO. These interactions affect the filling of states derived from Pd 4*d* near the edge of the valence band. The thickness of the Al_2O_3 barrier in S2 (6 nm) likely corresponds to a bonding regime that shifts E_g the most significantly compared to the thinnest and thickest Al_2O_3 barrier layers. However, it should be noted that the E_g values for S1+PdO (2.175 eV) and S3+PdO (2.176 eV) are almost indistinguishable within the error margin inherent to the Tauc method (~0.05 eV). Thus, the most significant E_g contrast is observed only between S2+PdO and the other two configurations.

The E_g values provide the basis for an accurate interpretation of the Z-scan results at both excitation wavelengths. At λ = 800 nm, the photon energy is $h\nu$ = 1.55 eV, which is significantly lower than E_g for all three PdO configurations. Therefore, the 800 nm excitation is strictly sub-bandgap for PdO in all samples, meaning that PdO contributes to $Re\chi^{(3)}$ exclusively through virtual transitions of bound electrons, which, according to the two-band Kramers-Kronig argument, yields a positive sign for $Re\chi^{(3)}$ [8]. At λ = 400 nm, the photon energy is $h\nu$ = 3.10 eV, which significantly exceeds the value of E_g(PdO) for all configurations. Thus, excitation at 400 nm is beyond the bandgap for PdO, activating real interband transitions and making $Im\chi^{(3)}$ the dominant nonlinear optical channel from PdO at this wavelength. This spectral dichotomy is the main physical difference between the two measurement modes and forms the basis for the subsequent analysis of nonlinear mechanisms.

In addition to the aforementioned changes in the bandgap width, the deposition of a 16-nm PdO layer induces spectrally selective changes in the optical density profiles (Fig. 1, dashed lines), which differ quantitatively for the three samples. At 400 nm, the PdO-induced increase in α_0 is approximately 4.7, 7.1, and 3.9 for S1, S2, and S3, respectively, while at 800 nm, the corresponding coefficients are 3.5, 2.5, and 2.6. Furthermore, the ratio ΔOD(400)/ ΔOD(800), which is 2.69, 5.02, and 3.25 for S1+PdO, S2+PdO, and S3+PdO, respectively, reflects a stronger spectral weight of PdO absorption at 400 nm compared to 800 nm in all configurations. Its non-monotonic dependence on the Al_2O_3 thickness is consistent with the competing roles of the near-field and barrier shielding discussed in Section 4.

The systematic red shift of the PdO absorption edge from ~350 nm in S1+PdO to ~395 nm in S2+PdO and ~448 nm in S3+PdO (Fig. 1) is consistent with the trend of E_g in the Tauc diagram and further confirms the picture of the modification of the PdO electronic structure under the influence of the barrier. In S3+PdO, the edge of the absorption band at 448 nm is closest to the 400 nm laser wavelength among the three configurations, creating an additional absorption channel above the bandgap width at this wavelength.

The values of α_0 at 400 and 800 nm for all six configurations, obtained from the spectra, are given in Table 1.

Table 1. Structural and linear optical characteristics of Ag/AuNP-Al_2O_3-PdO multilayer configurations.

Sample	**Al_2O_3 (nm)**	**L (nm)**	**α_0(800 nm) (cm^{-1})**	**α_0(400 nm) (cm^{-1})**	**λ_{LSPR} (nm)**
S1	1.5	9.1	24513.143	170451.803	409, 513
S1+PdO	1.5	25.1	86934.567	376012.114	-

S2	6.0	13.6	24362.413	188066.216	414, 517
S2+PdO	6.0	29.5	39259.313	320251.406	-
S3	12.0	19.6	1072.555	80050.742	466
S3+PdO	12.0	35.6	48795.151	299955.233	-

3.2 Nonlinear optical response at 800 nm

The nonlinear optical parameters obtained from Z-scans using femtosecond pulses at a wavelength of 800 nm for all six sample configurations are presented in Table 2.

Table 2. Nonlinear optical parameters of Ag/AuNP-Al_2O_3 and Ag/AuNP-Al_2O_3-PdO structures measured under femtosecond 800 nm irradiation of variable intensity, grouped by Al_2O_3 thickness.

Sample	**n_2 (cm^2/W)**	**β (cm/W)**	**I_s (GW/cm^2)**	**Re$\chi^{(3)}$ (esu)**	**Im$\chi^{(3)}$ (esu)**	**$\lvert\chi^{(3)}\rvert$ (esu)**	**$\lvert\chi^{(3)}\rvert$ Enhancement**
S1	-5.93×10^{-11}	0.51×10^{-5}	350	-0.99×10^{-11}	0.73×10^{-11}	1.23×10^{-11}	-
S1+PdO	-7.12×10^{-11}	0.90×10^{-5}	61	-5.70×10^{-9}	**6.11×10^{-9}**	**8.35×10^{-9}**	**×679**
S2	$+6.28\times10^{-11}$	0.80×10^{-5}	109	$+1.05\times10^{-11}$	1.13×10^{-11}	1.55×10^{-11}	-
S2+PdO	**$+3.01\times10^{-10}$**	1.1×10^{-5}	65	**$+2.41\times10^{-8}$**	7.46×10^{-9}	**2.52×10^{-8}**	**×1625**
S3	-0.81×10^{-11}	0.75×10^{-5}	50	-6.48×10^{-10}	5.09×10^{-9}	5.13×10^{-9}	-
S3+PdO	**$+5.31\times10^{-11}$**	0.5×10^{-5}	310	**$+4.25\times10^{-9}$**	1.70×10^{-9}	4.57×10^{-9}	**×4**

Typical OA and CA curves from the Z-scans are shown in Figure 3. It should also be noted that the probe wavelength of 800 nm lies in the off-resonance spectral region for all uncoated samples. Moreover, the photon energy $h\nu$ = 1.55 eV is significantly smaller than the bandgap width of the top PdO layer for all samples (E_g = 2.18-2.24 eV).

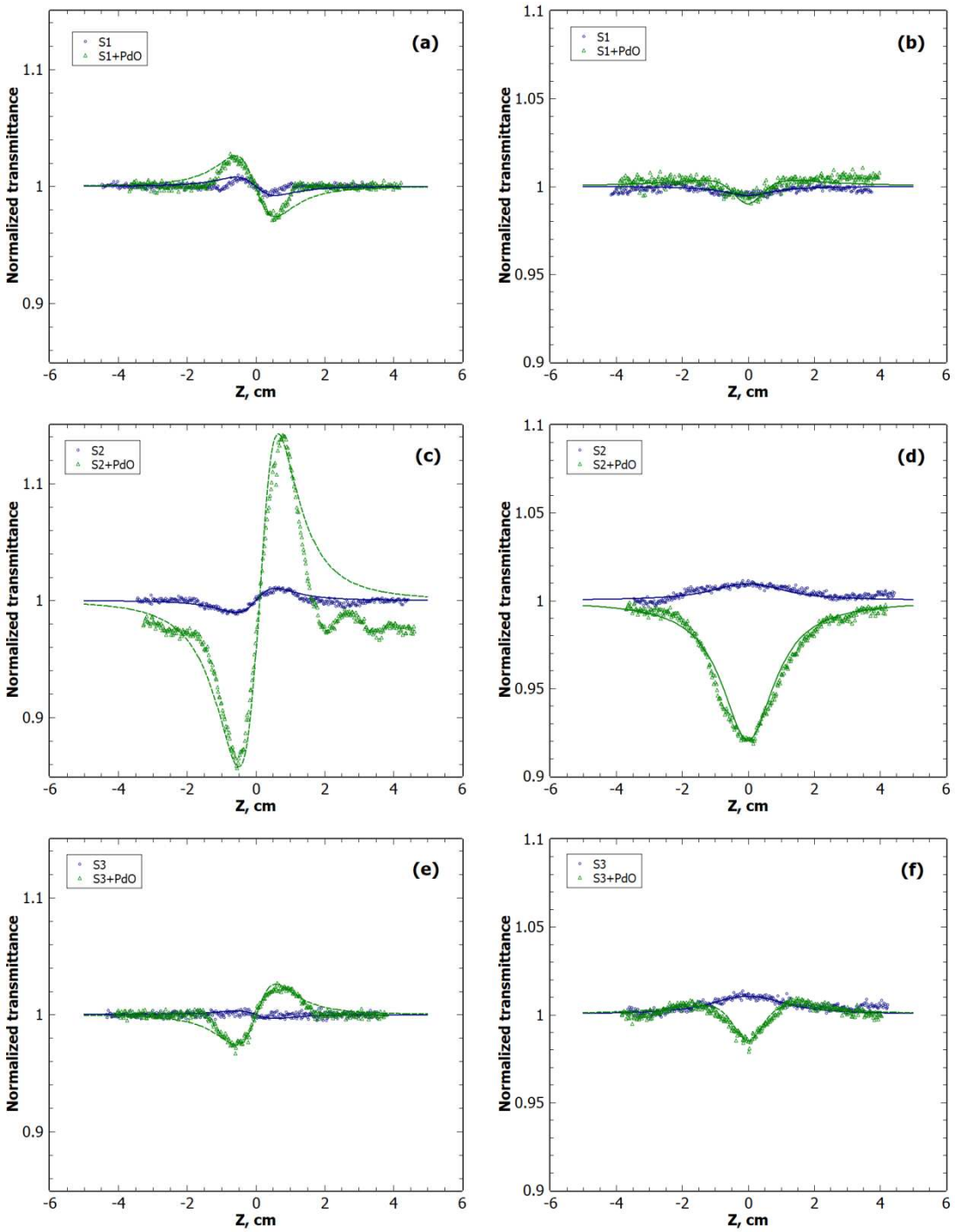


Fig. 3 Normalized Z-scan traces at 800 nm for Ag/AuNP-Al_2O_3 (solid lines) and Ag/AuNP-Al_2O_3-PdO (dashed lines). (a, c, e) Closed-aperture (CA); (b, d, f) open-aperture (OA). Panels (a, b) S1 (1.5 nm Al_2O_3), (c, d) S2 (6 nm Al_2O_3), (e, f) S3 (12 nm Al_2O_3). Solid curves are fits to the Kwak et al. model [18] (CA) and the two-mechanism Zhang et al. model [19] (OA)

As a result of CA Z-scanning for samples S1, S2, and S3 without PdO coating, nonlinear refractive indices of n_2 = -5.93×10^{-11}, $+6.28\times10^{-11}$, and -0.81×10^{-11} cm^2/W were obtained, respectively. The negative sign of n_2 in samples S1 and S3 is consistent with the Kerr's mechanism of in-band excitation of quasi-free conduction electrons in Ag/Au nanoparticles. Their intensity-dependent redistribution within the conduction band modifies the effective dielectric function and results in a negative value of $Re\chi^{(3)}$ in the non-resonant spectral region [6, 7]. A positive value of n_2 for sample S2 without PdO ($+6.28\times10^{-11}$ cm^2/W) turned out to be an exception for the series of uncoated samples. This positive sign at an intermediate Al_2O_3 layer thickness is consistent with the

non-monotonic dependence of $Re\chi^{(3)}$ on $d(Al_2O_3)$, reported in [9] for both femtosecond and nanosecond excitation regimes. It was found there that intermediate barrier thicknesses promote a positive nonlinear refractive response; the exact mechanism remains to be determined.

The data obtained from OA Z-scanning of samples without a PdO coating show relatively weak nonlinear changes in absorption. The OA curves exhibit a characteristic two-component shape. Relatively far from the focus, an increase in transmittance is observed, indicating a saturated absorption (SA) mechanism, while in the focal plane or near it, a local minimum in transmittance is observed, indicating a reverse saturated absorption (RSA) mechanism. This competition between SA and RSA yields nonlinear absorption coefficients $\beta = 0.51\text{-}0.75\times10^{-5}$ cm/W and saturation intensities $I_s = 50\text{-}350$ GW/cm^2 for the three uncoated samples. The SA component is explained by the depletion of the LSPR ground state. Apparently, at a wavelength of 800 nm, despite off-resonance conditions, the low-energy tail of the plasmon resonance retains sufficient oscillator strength to sustain partial depletion of the ground state under the action of intense femtosecond excitation. The RSA component near the focal plane is possibly associated with excited-state absorption (ESA) of transiently excited "hot" charge carriers, which is consistent with the known ultrafast dynamics of "hot spot"-type plasmonic structures [20]. The relatively high values of I_s (50-350 GW/cm^2) confirm that both mechanisms operate well below the saturation level at the laser pulse intensities used.

Z-scan investigations of samples with a deposited PdO top layer revealed qualitatively different effects in all three samples, as summarized in Table 2. The most significant result at 800 nm is the change in the sign of n_2 in sample S3. After PdO deposition, the value of n_2 in this sample changes from -0.81×10^{-11} to $+5.31\times10^{-11}$ cm^2/W, with the change in sign accompanied by a 6.6-fold increase in magnitude. In sample S1, the sign of n_2 remains negative, and its value increases slightly from -5.93×10^{-11} to -7.12×10^{-11} cm^2/W. In sample S2, the sign remains positive, and n_2 increases by a factor of 4.8: from $+6.28\times10^{-11}$ to $+3.01\times10^{-10}$ cm^2/W. Thus, the sign of n_2 remains the same in samples S1 and S2 but changes to the opposite in S3, indicating a clear dependence of the PdO-induced changes in $Re\chi^{(3)}$ on the thickness of the Al_2O_3 barrier.

The OA Z-scan curves for PdO-coated sample configurations retain the two-component SA+RSA spectral shape observed in uncoated samples, but with markedly different relative contributions from these two mechanisms depending on the Al_2O_3 thickness. The $Im\chi^{(3)}$ values, calculated based on the determined β values, increase significantly after PdO deposition. For the S1+PdO sample, the $Im\chi^{(3)}$ value increased approximately 84-fold, and 66-fold for the S2+PdO sample, whereas the increase for S3+PdO is significantly smaller. This increase in the $Im\chi^{(3)}$ values can be explained by the enhancement of both the SA and RSA channels due to the plasmon-enhanced near-field between the Ag/Au and PdO nanoparticles. The intense local field on the surface of the nanoparticles increases the effective excitation density in PdO, enhancing the depletion of the ground state and simultaneously promoting the filling of the excited state accessible to ESA. This near-field enhancement is most effective across the thin and intermediate barriers S1 and S2, where the direct electromagnetic coupling between the nanoparticles and PdO is strongest, and decreases significantly at S3, where a 12-nm-thick barrier partially shields the PdO from the nanoparticles' near field.

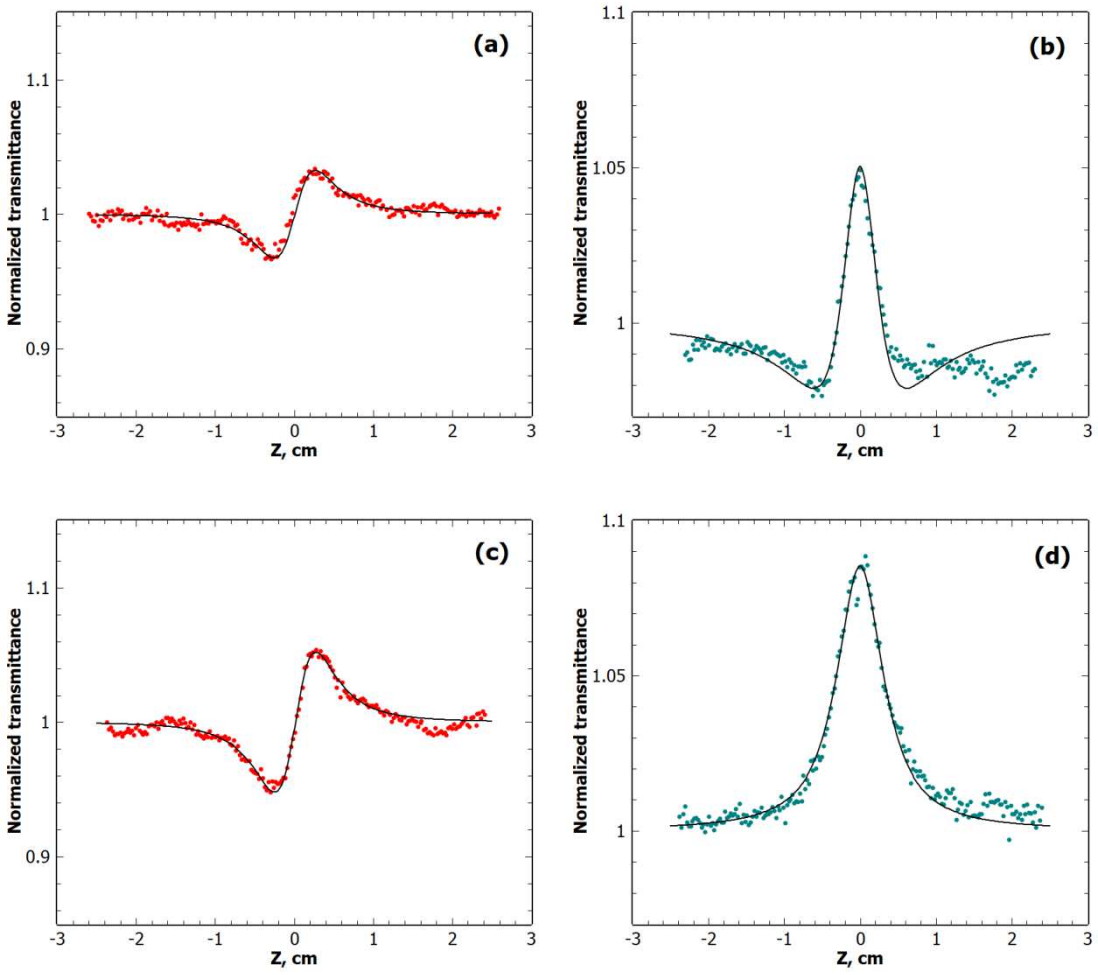
The total value of $|\chi^{(3)}|$ increases by approximately 679 times (S1) and 1625 times (S2) after PdO deposition. The data in Table 2 show that in both S1+PdO and S2+PdO, $Im\chi^{(3)}$ significantly exceeds $Re\chi^{(3)}$. Thus, for S1+PdO, $Im\chi^{(3)} = 6.11\times10^{-9}$ esu versus $Re\chi^{(3)} = -5.70\times10^{-9}$ esu; the same advantage is observed for S2+PdO. Therefore, it should be clearly noted that such a significant enhancement of $|\chi^{(3)}|$ does not reflect a proportional enhancement of nonlinear refraction but is primarily due to strong nonlinear absorption. As previously noted, this enhancement of nonlinear

absorption arises from plasmon-mediated near-field interactions between Ag/Au nanoparticles and PdO. The much smaller enhancement factor in S3+PdO is likely consistent with the fact that the thick barrier significantly reduces these interactions.

The saturation intensity I_s decreases significantly after PdO deposition in all three samples. Specifically, for S1, the I_s value decreased from 350 to 61 GW/cm^2, while for S2 and S3, the decrease is smaller. This indicates that the configuration with a thin Al_2O_3 barrier is the most effective for lowering the saturation threshold, which is consistent with the strongest NP-PdO electromagnetic coupling at d(Al_2O_3) = 1.5 nm.

3.3 Nonlinear optical response at 400 nm

The nonlinear optical parameters of each PdO-coated sample at a wavelength of 400 nm were determined using the OA and CA Z-scan techniques for four values of I_0 in the range 9.43-37.72 W/cm^2. Typical Z-scan curves are shown in Fig. 4. As established in Section 3.1, the laser wavelength of 400 nm lies in a region close to the LSPR resonance in samples S1 (409 nm) and S2 (414 nm), and overlaps the optical bandgap of PdO ($h\nu$ = 3.10 eV > E_g = 2.18-2.24 eV) for all samples. This combination of plasmonic, interband, and extra-band excitation channels makes the 400 nm range qualitatively richer than the 800 nm range, and provides a markedly different non-linear response in the samples under investigation.



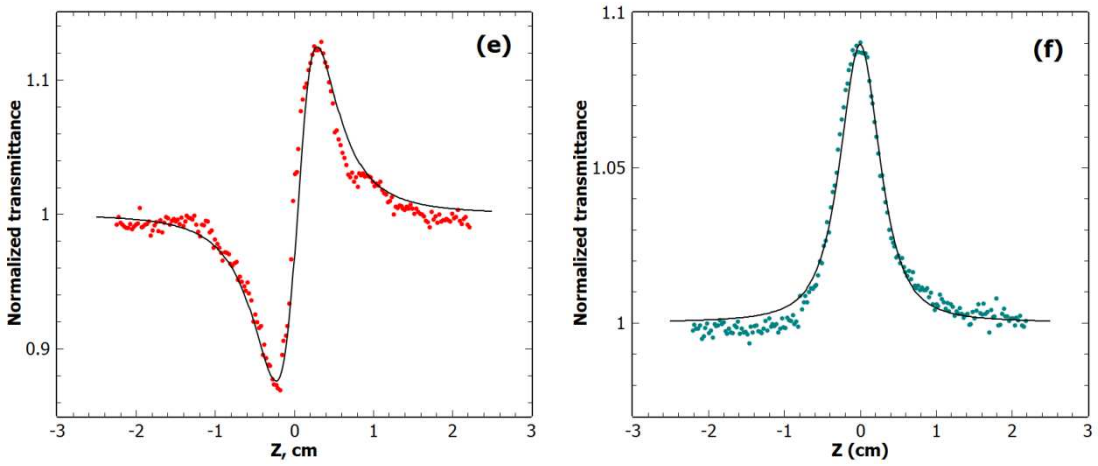


Fig. 4 Normalized Z-scan traces at 400 nm for Ag/AuNP-Al_2O_3-PdO structures. (a, c, e) Closed-aperture (CA); (b, d, f) open-aperture (OA). (a, b) S1+PdO (1.5 nm Al_2O_3), (c, d) S2+PdO (6 nm Al_2O_3), (e, f) S3+PdO (12 nm Al_2O_3). Solid lines, fits to the theoretical model

The open-aperture Z-scan OA curves for all samples demonstrate an increase in transmittance as the focus is approached, which is a typical indication of saturation absorption (SA). While the experimental results for samples S2 and S3 can be approximated relatively well using a standard single-component model of weak saturation, this model is not optimal for sample S1. It is presumed that the observed line shapes require the simultaneous presence of both an SA-like and a 2PA/RSA-like nonlinear absorption channel. Using Equation 5 to fit the OA data significantly improved the fit, confirming the presence of such a competing absorption channel. This makes physical sense: with a relatively thin dielectric layer of 1.5 nm, direct tunneling/charge transport in PdO likely opens up an additional, broad RSA-like loss channel, which partially compensates for the intrinsic bleaching of the islands. With a thicker Al_2O_3 layer, this channel disappears.

Table 3. Nonlinear optical parameters of Ag/AuNP-Al_2O_3-PdO structures measured under femtosecond 400 nm irradiation of variable intensity, grouped by Al_2O_3 thickness.

I_0(GW/cm²)	n_2 (cm²/W)	β (cm/W)	I_s (GW/cm²)	Re$\chi^{(3)}$ (esu)	Im$\chi^{(3)}$ (esu)	$\lvert\chi^{(3)}\rvert$ (esu)
S1+PdO (Al_2O_3 = 1.5 nm, thin barrier)						
9.43	7.5×10^{-11}	9.5×10^{-6}	150	9.13×10^{-9}	4.90×10^{-9}	10.36×10^{-9}
15.71	3.8×10^{-11}	6.5×10^{-6}	190	4.62×10^{-9}	3.36×10^{-9}	5.71×10^{-9}
25.14	2.7×10^{-11}	6.0×10^{-6}	215	3.29×10^{-9}	3.10×10^{-9}	4.52×10^{-9}
37.72	1.8×10^{-11}	5.0×10^{-6}	250	2.19×10^{-9}	2.58×10^{-9}	3.39×10^{-9}
S2+PdO (Al_2O_3 = 6 nm, intermediate barrier)						
9.43	15×10^{-11}	3.0×10^{-6}	65	18.26×10^{-9}	1.55×10^{-9}	18.32×10^{-9}
15.71	6.2×10^{-11}	0.1×10^{-6}	350	7.55×10^{-9}	5.16×10^{-11}	7.55×10^{-9}
25.14	4.0×10^{-11}	1.0×10^{-6}	220	4.87×10^{-9}	0.52×10^{-9}	4.90×10^{-9}
37.72	2.6×10^{-11}	1.0×10^{-6}	214	3.16×10^{-9}	0.52×10^{-9}	3.21×10^{-9}
S3+PdO (Al_2O_3 = 12 nm, thick barrier)						
9.43	4.0×10^{-11}	3.0×10^{-6}	118	4.86×10^{-9}	1.55×10^{-9}	5.11×10^{-9}
15.71	6.9×10^{-11}	1.0×10^{-6}	125	8.4×10^{-9}	0.52×10^{-9}	8.41×10^{-9}
25.14	6.8×10^{-11}	1.5×10^{-6}	160	8.28×10^{-9}	0.77×10^{-9}	8.31×10^{-9}
37.72	6.2×10^{-11}	2.0×10^{-6}	180	7.53×10^{-9}	1.03×10^{-9}	7.6×10^{-9}

When the determined nonlinear parameters are compared with those presented in [9] for similar samples without a PdO coating at a wavelength of 400 nm ($n_2 = 6.30\times10^{-10}$, 5.12×10^{-10} and 4.80×10^{-10} cm^2/W and $\beta = 3.2\text{-}7.25\times10^{-5}$ cm/W for S1, S2 and S3, respectively), it is evident that the PdO-coated samples exhibit n_2 values that are 3-6 times lower, as well as a sharp decrease in β. This suggests that the presence of the PdO coating layer fundamentally alters the nonlinear absorption mechanism from predominantly RSA (without PdO) to predominantly SA (with PdO) across the entire series of samples.

As shown in Table 3, the nonlinear refractive index n_2 of sample S1 decreases monotonically as I_0 increases, from 7.5×10^{-11} cm^2/W at $I_0 = 9.43$ GW/cm^2 to 1.8×10^{-11} cm^2/W at $I_0 = 37.72$ GW/cm^2. This is consistent with the progressive bleaching of the ground state. Clearly, at higher intensities, a greater proportion of charge carrier's transition to the excited state, reducing the available absorption cross section and diminishing the effective nonlinear response. Furthermore, the saturation intensity (I_s) increases monotonically from 150 GW/cm^2 to 250 GW/cm^2 across the entire studied range, reflecting the gradual exhaustion of available absorption states. At higher I_0 values, a larger proportion of states are already occupied, raising the apparent saturation threshold. For S1, the nonlinear absorption coefficient $\beta = 9.5\text{-}5.0\times10^{-6}$ cm/W is significant. This decreases with increasing I_0, indicating the presence of an absorption channel that competes with the SA channel. This was identified using an extended 2PA approximation. This behavior is physically consistent with an ultrathin Al_2O_3 barrier (1.5 nm). At this barrier thickness, direct tunneling with charge transfer from the Ag/Au nanoparticles to the PdO traps is most efficient. This opens up an additional channel of absorption losses that competes with LSPR bleaching and partially suppresses the SA signal. As I_0 increases, the traps are likely to become saturated, and this competing channel will weaken, which is consistent with the decreasing dependence of $\beta(I_0)$. Accordingly, $Im\chi^{(3)}$ and $|\chi^{(3)}|$ decrease from 4.90×10^{-9} and 10.36×10^{-9} esu at $I_0 = 9.43$ GW/cm^2 to 2.58×10^{-9} and 3.39×10^{-9} esu at $I_0 = 37.72$ GW/cm^2.

The nonlinear response of S2 is characterized by the most anomalous dependence of I_s on I_0 of all the samples in the series. At the lowest intensity ($I_0 = 9.43$ GW/cm^2), I_s is significantly lower than for S1 at 65 GW/cm^2, with the highest $Re\chi^{(3)}$ of 18.26×10^{-9} esu and $|\chi^{(3)}|$ of 18.32×10^{-9} esu among all configurations and intensities. At $I_0 = 15.71$ GW/cm^2, I_s rises sharply to 350 GW/cm^2, gradually decreasing to 214 GW/cm^2 at $I_0 = 37.72$ GW/cm^2. This non-monotonic threshold behavior of I_s may indicate a two-stage saturation dynamic, which has not been observed in either S1 or S3 and which represents a new effect for Ag/Au-oxide heterostructures. This can be interpreted as the sequential saturation of two physically distinct absorbing subsystems with different saturation thresholds. At low I_0 values, the interfacial trap states at the Ag/Au-Al_2O_3 interface, enhanced by the near-field of the low-frequency plasmon, saturate first, resulting in low visible I_s. Above the threshold intensity, these states become completely depleted and the dominant absorption channel shifts to the bulk PdO, which has a higher saturation threshold. This causes a sharp increase in I_s. The subsequent gradual decrease may reflect the partial recovery of the ground state or additional nonlinear processes. The nonlinear absorption coefficient β exhibits a correlated anomaly: $\beta = 3.0\times10^{-6}$ cm/W at $I_0 = 9.43$ GW/cm^2, dropping sharply to 0.1×10^{-6} cm/W at $I_0 = 15.71$ GW/cm^2, which coincides exactly with the Is threshold, and recovering to ~1.0×10^{-6} cm/W at higher I_0 values. This correlated behavior of I_s and β at the threshold point strongly supports the interpretation of sequential saturation. The dependence $n_2(I_0)$ decreases from 15×10^{-11} cm^2/W to 2.6×10^{-11} cm^2/W, which follows the approximate inverse dependence characteristic of $\chi^{(3)}$ saturation. This is caused by the progressive bleaching of the ground state in a quantum-confined plasmonic system [13].

The nonlinear response of S3 is characterized by the non-monotonic dependence of n_2 on I_0. The n_2 rises from 4.0×10^{-11} cm^2/W at $I_0 = 9.43$ GW/cm^2 to a maximum of 6.9×10^{-11} cm^2/W at $I_0 =$

15.71 GW/cm^2, before gradually decreasing to 6.2×10^{-11} cm^2/W at I_0 = 37.72 GW/cm^2. The presence of a maximum value of n_2 at an intermediate intensity is indicative of competing refractive contributions. At low I_0 values, the positive real part of the third-order susceptibility (Re$\chi^{(3)}$) from the Ag/Au low-frequency (LF) mode and the sub-zone-bound electronic response of PdO increases with intensity. Above the threshold, progressive bleaching of the ground state and the onset of supra-zone absorption channels in PdO begin to reduce the Re$\chi^{(3)}$ contribution, resulting in the observed saturation. The saturation intensity (I_s) increases monotonically from 118 GW/cm² to 180 GW/cm^2, reflecting the progressive saturation of the SA channel, independent of the threshold dynamics characteristic of S2. The nonlinear absorption coefficient β, is present across the entire intensity range and exhibits non-monotonic dependence, with values of 1.0-3.0×10^{-6} cm/W. It decreases from 3.0×10^{-6} cm/W at I_0 = 9.43 GW/cm^2 to a minimum of 1.0×10^{-6} cm/W at I_0 = 15.71 GW/cm^2, before increasing to 2.0×10^{-6} cm/W at I_0 = 37.72 GW/cm^2. This mirrors the non-monotonicity of $n_2(I_0)$. The correlated behavior of n_2 and β is consistent with the Kramers-Kronig relation: the maximum of Re$\chi^{(3)}$ coincides with the minimum of Im$\chi^{(3)}$ as expected when the dominant resonant contribution to $\chi^{(3)}$ passes through its peak. This enables the accumulation of an excited state, which, according to the Kramers-Kronig theory [20], drives the correlated behavior of n_2 and β. The maximum values of Re$\chi^{(3)}$ and $|\chi^{(3)}|$ are 8.40×10^{-9} and 8.41×10^{-9} esu, respectively, at I_0 = 15.71 GW/cm^2.

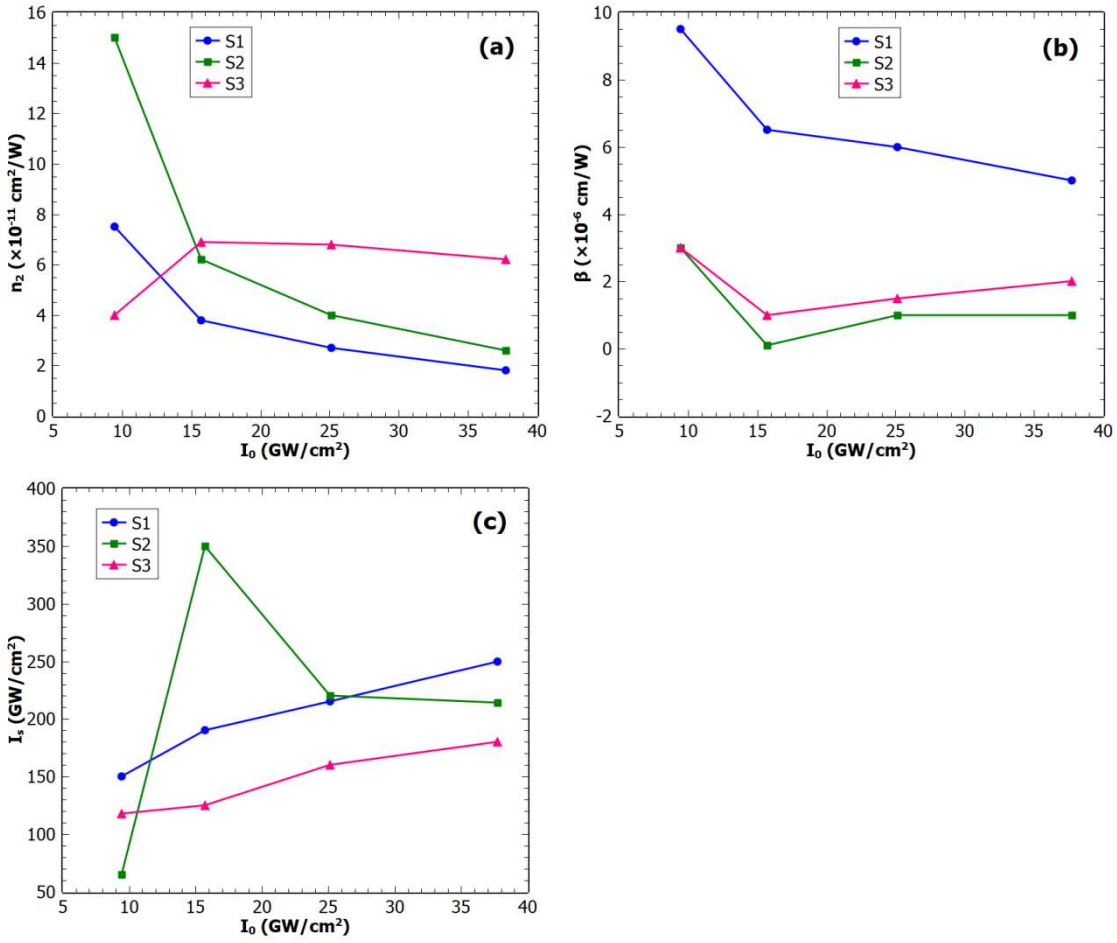


Fig. 5 Intensity dependence of the nonlinear refractive index n_2 (a), two-photon absorption coefficient β (b), and saturation intensity I_s (c) for Ag/AuNP-Al_2O_3-PdO structures at 400 nm

Figure 5 shows the dependences of n_2, I_s, and β on I_0 at a wavelength of 400 nm for all samples, which show qualitatively different behaviors. Although all samples show a general trend of decreasing n_2 at high I_0 values, they differ significantly in their absorption dynamics. S1 shows a monotonic decrease in β due to saturation of trap states caused by the narrow barrier. S2 shows a

jump in the I_s threshold and a correlated minimum in β at the same I_0. S3 shows non-monotonic curves of $n_2(I_0)$ and $\beta(I_0)$, which are related by the Kramers-Kronig relation due to the confinement of carriers by the thick barrier. The maximum $|\chi^{(3)}|$ at a wavelength of 400 nm is 18.32×10^{-9} esu for S2 at I_0 = 9.43 GW/cm^2. This is the highest value recorded in this study at this wavelength, and it exceeds by more than an order of magnitude the $|\chi^{(3)}|$ value reported for a similar configuration without PdO coating in reference [1].

4. Discussion

The results presented in Section 3 cover two qualitatively distinct excitation modes, and understanding their differences is essential for their correct interpretation. At 800 nm, all three samples are excited in the transparency window outside the resonance of Ag/Au nanoparticles, and hν = 1.55 eV is a strictly sub-bandgap value for PdO (E_g = 2.175-2.240 eV). Thus, the nonlinear optical response is determined exclusively by virtual electronic transitions in both components of the samples. At 400 nm, three independent channels of optical nonlinearity can be simultaneously activated: the proximity to the LSPR of samples S1 (409 nm) and S2 (414 nm), the tail of the Au interband absorption extending to ~400 nm [12], and real transitions in PdO above the bandgap width (hν = 3.10 eV >> E_g). However, the condition of proximity to the 400 nm resonance is not satisfied equally for all samples: the short-wavelength LSPR peaks of samples S1 and S2 lie within 5-14 nm of the wavelength of the probing laser radiation, whereas the combined resonance of sample S3 is shifted by ~ 66 nm. Since $\chi^{(3)}$ depends on the local field amplification factor to the fourth power ($\chi^{(3)} \propto |f_{loc}|^4$) [9], these spectral relationships underlie the observed hierarchy of $|\chi^{(3)}|$ values at 400 nm. This also explains the anomalously large ratio ΔOD(400)/ΔOD(800) for S2+PdO (5.02 versus 2.69 and 3.25 for S1 and S3). Thus, it is confirmed that the S2 LSPR at 414 nm provides the strongest resonant interaction between the near-field of the nanoparticle and the PdO absorption states at this wavelength.

The most significant result at a wavelength of 800 nm is the PdO-induced change in the sign of n_2 in S3 from -0.81×10^{-11} to $+5.31\times10^{-11}$ cm^2/W. We assume that the effective value of $\mathrm{Re}\chi^{(3)}$ for the composite system is a superposition of contributions from the metal nanoparticles and the PdO, each weighted by the local field enhancement factor:

$$Re\chi^{(3)}_{eff} = f_{metal} Re\chi^{(3)}_{e} + f_{PdO} Re\chi^{(3)}_{PdO} \quad (9)$$

where f_i is the effective volume fraction, weighted by $|f_{loc}|^4$, and the contribution of Al_2O_3 is negligible due to the large bandgap width and low polarizability [9]. The first term, $Re\chi^{(3)}_e$, arises from the in-band Kerr optical effect of quasi-free conduction electrons in Ag/Au nanoparticles, which yields a negative value of $Re\chi^{(3)}$ in the transparency window outside the resonance [5, 6]. This is consistent with the negative value of n_2 for S1 and S3 without PdO. The positive value of n_2 for S2 without PdO corresponds to the non-monotonic dependence of the sign on $d(Al_2O_3)$, as reported in [1]. The exact mechanism underlying this sign change has yet to be established. The second term, $Re\chi^{(3)}_{PdO}$, arises from virtual transitions of bound electrons in PdO at 800 nm. Since hν = 1.55 eV < E_g, PdO is excited below the bandgap at this wavelength. According to the two-band model and the Kramers-Kronig relations for nonlinear susceptibility [8], a semiconductor excited below its bandgap acquires a positive $Re\chi^{(3)}$, whose magnitude is proportional to the two-photon absorption coefficient at twice the photon energy. Since $2h\nu$ = 3.10 eV > E_g and the two-photon resonance condition is satisfied, this makes $Re\chi^{(3)}_{PdO}$ both positive and quite significant. These two features constitute a key distinction from the negative $Re\chi^{(3)}_e$ of metallic nanoparticles.

The balance between these two contributions is controlled by d(Al_2O_3) through the hot-carrier tunneling probability, which scales as *exp(-2kd)* with $k \sim 5\text{-}8$ nm^{-1} for amorphous Al_2O_3 [20]. In S1 (d = 1.5 nm), efficient tunnelling from the NPs into PdO trap states screens the PdO contribution and maintains the dominance of $Re\chi^{(3)}_e$ - the sign of n_2 remains negative after PdO deposition. In S2 (d = 6 nm), partial coupling allows $Re\chi^{(3)}_{PdO}$ to add positively to an already positive $Re\chi^{(3)}_e$, amplifying n_2 without sign change. In S3 (d(Al_2O_3) = 12 nm), the thick barrier suppresses tunneling by more than sixty orders of magnitude relative to d(Al_2O_3) = 1.5 nm, confining hot carriers within the NPs and allowing the full sub-gap $Re\chi^{(3)}_{PdO}$ to contribute unscreened. Since $Re\chi^{(3)}_e$ is the smallest in absolute value among the three uncoated samples ($n_2 = -0.81\times10^{-11}$ cm^2/W), the positive $Re\chi^{(3)}_{PdO}$ dominates the superposition and reverses the sign.

The significant increase in $|\chi^{(3)}|$ (by ~679 times for S1 and ~1625 times for S2) following PdO deposition at 800 nm is a distinct effect that requires careful analysis. As shown in Table 2, in both S1+PdO and S2+PdO, $Im\chi^{(3)}$ significantly exceeds $Re\chi^{(3)}$; therefore, the enhancement of $|\chi^{(3)}|$ does not reflect a proportional enhancement of nonlinear refraction but is primarily due to significant nonlinear absorption arising from the plasmon-enhanced near-field between Ag/AuNPs and PdO. The intense local field on the surface of the NP, amplified by the scaling $|f_{loc}|^4$, sharply increases the effective excitation density absorbed by PdO, while simultaneously enhancing both the SA and RSA absorption channels. This near-field enhancement is most effective through the thin and intermediate barriers S1 and S2, where the direct electromagnetic coupling between the NP and PdO is strongest. At the same time, it decreases significantly in S3, where a 12 nm-thick barrier shields PdO from the near-field of the NP. This is consistent with the significantly lower gain factor in S3 (~4). Thus, the usefulness of the S1+PdO and S2+PdO systems for practical applications at a wavelength of 800 nm lies primarily in their significant nonlinear absorption, rather than in enhanced nonlinear refraction, which has direct implications for the design of optical limiters and saturable absorbers [17].

The hot carrier transport speed is controlled by the thickness of the Al_2O_3 barrier. This is a factor that determines the sign and magnitude of $Re\chi^{(3)}$ at 800 nm. It also determines the nonlinear absorption mechanism at 400 nm. This provides a unified picture for both wavelengths. At 400 nm, PdO excitation above the bandgap width generates hot carriers both in Ag/Au nanoparticles and directly in PdO. In the S1+PdO and S2+PdO samples, thin and intermediate barriers allow for rapid tunneling of photogenerated carriers from the nanoparticles into surface and defect states of PdO, depleting the metal's excited-state population in less than a picosecond, rapidly restoring the ground state and making SA the dominant mechanism. This carrier transfer also explains the sharp decrease in β following PdO deposition (from $\sim10^{-5}$ cm/W without PdO to $\sim10^{-6}$ cm/W with PdO) across the entire series of samples. Here, PdO acts as a charge transfer acceptor that depletes the excited states responsible for RSA in the uncoated Ag/Au-Al_2O_3 system [9]. The additional 2PA-like channel detected in S1+PdO is physically consistent with the thinnest Al_2O_3 barrier (1.5 nm). At this thickness, the interlayer coupling between the Ag/AuNPs and PdO, with charge transfer to PdO, opens up a broad additional loss channel that competes with LSPR bleaching, which weakens with increasing I_0 and saturation of the PdO trap states. This is consistent with the monotonic decrease in $\beta(I_0)$. In S3+PdO, a 12 nm-thick barrier effectively suppresses tunneling, trapping hot carriers inside the nanoparticles throughout the entire pulse. This restriction allows the excited-state population to accumulate. This leads to the coexistence of SA and RSA, as evidenced by the nonzero value of β across the entire intensity range, as well as the non-monotonic dependence of $n_2(I_0)$, which is characteristic of this particular configuration.

The sharp increase in I_s observed in S2+PdO at $I_0 \sim 15$ GW/cm^2 (from 65 to 350 GW/cm^2), accompanied by a simultaneous sharp decrease in β, is a nonlinear optical phenomenon

characteristic of an intermediate-barrier configuration. We interpret this as the sequential saturation of two physically distinct absorption subsystems. At low intensities, saturation predominantly occurs in interphase trap states at the Ag/Au-Al_2O_3 interface due to the 6 nm barrier thickness, and these states are the most abundant in S2. This provides sufficient electromagnetic coupling for near-field amplification and sufficient physical confinement to prevent the immediate outflow of charge carriers. At the same time, the low saturation threshold ($I_s \approx 65$ GW/cm^2) reflects the enhancement of the effective absorption cross section in the near field, while the associated high value of β reflects losses in this channel. Once these interphase states have been completely depleted at $I_0 \sim 15$ GW/cm^2, absorption predominantly occurs in the bulk PdO, which has a higher saturation threshold ($I_s \approx 350$ GW/cm^2). This reflects its higher density of states and weaker near-field. The sharp drop in β from 3.0×10^{-6} to 0.1×10^{-6} cm/W is a direct consequence of this change in dominant absorption channel. RSA-type losses from the interphase channel disappear after complete bleaching, and the bulk PdO then operates in pure SA mode. The subsequent recovery of β at higher values of I_0 indicates the gradual onset of absorption above the threshold level in the PdO channel. This two-step dynamics places S2+PdO at an optimal intermediate point between the strong coupling in S1 (which prevents the accumulation of traps at the interface) and the strong blocking in S3 (which eliminates the enhancement of interphase states in the near field).

The non-monotonic and mirror-image dependencies of $n_2(I_0)$ and $\beta(I_0)$ in S3+PdO reach their extremes at an intensity of $I_0 = 15.71$ W/cm^2, which directly manifests the Kramers-Kronig relations that link $Re\chi^{(3)}$ and $Im\chi^{(3)}$ in the presence of a resonant nonlinear transition [8]. At low values of I_0, the positive value of $Re\chi^{(3)}$ from Ag/Au nanoparticles and the response due to bound PdO electrons in the region below the bandgap width both increase with intensity, contributing to an increase in n_2. At the same time, the accumulation of confined hot carriers fills the excited states and increases β.

At $I_0 = 15.71$ GW/cm^2, filling of the excited states reaches a maximum within the pulse duration, and $Re\chi^{(3)}$ also reaches a maximum due to dispersion of the excited-state resonance as determined by the Kramers-Kronig relations. Above this intensity, the progressive depletion of the ground state and the emergence of absorption channels above the bandgap width in PdO reduce $Re\chi^{(3)}$, leading to a decrease in n_2. At the same time, saturation during the transition to the excited state reduces β.

The correlated changes in these two quantities at a constant I_0 value are consistent with the anomalous ultrafast dynamics of confined hot plasmon carriers, as reported by Harutyunyan et al. [20].

When the obtained results are considered in the context of published data (Table 6), the value $|\chi^{(3)}| = 2.52\times10^{-8}$ esu for S2+PdO at 800 nm exceeds by approximately 1.5 orders of magnitude the values reported for bilayer Ag/Au thin films at the same wavelength [21], and similarly exceeds $|\chi^{(3)}|$ for PdO films under nanosecond excitation [14]. Compared to Ag/Au-Al_2O_3 sample configurations without a PdO layer from [9], where $|\chi^{(3)}|$ at 800 nm lies in the range of 0.86-1.09×10^{-11} esu, the enhancement in S2+PdO induced by the PdO coating is ~ 1625. At 400 nm, the maximum value of $|\chi^{(3)}| = 18.32\times10^{-9}$ esu for S2+PdO exceeds, by more than an order of magnitude, the values reported for the corresponding configuration without a PdO coating in [9], and is comparable to the values reported for systems with strong absorption and quantum confinement, such as CdS nanoparticles [16]. This places the Ag/AuNP-Al_2O_3-PdO heterostructure in the same class of nonlinear characteristics, with the functionality of an inorganic, thermally stable thin-film platform.

Table 6. Comparison of third-order nonlinear optical parameters of Ag/AuNP-Al_2O_3–PdO heterostructures with literature data for related plasmonic systems. All values are for femtosecond excitation unless noted otherwise; results of this work are highlighted in bold.

System	λ (nm)	τ_p	n_2 (cm^2/W)	β (cm/W)	$\lvert\chi^{(3)}\rvert$ (esu)	Ref.
Ag/Au alloy NPs, colloidal	800	100 fs	$\sim -10^{-9}$	$\sim 10^{-5}$	$\sim 10^{-10}$	[22]
Ag@Au bimetallic NPs, colloidal	1040	~357 fs	$\sim -10^{-10}$	-	$\sim 10^{-11}$	[23]
Au@Ag core-shell NPs, colloidal	800	~100 fs	positive	negative	$\sim 10^{-10}$	[24]
AuNP in fluoroborate glass	813	~100 fs	$+1.85\times10^{-10}$	3.8×10^{-11}	2.37×10^{-14}	[25]
AgNP triangles, colloidal	400-800	~100 fs	SA + RSA	-	$\sim 10^{-10}$-10^{-9}	[26]
Ag/Al_2O_3/PVA nanocomposite	532	9 ns	-	-	$\sim 10^{-6}$	[27]
S1+PdO (Al_2O_3=1.5 nm)	**800**	**176 fs**	**-7.12×10^{-11}**	**0.9×10^{-5}**	**8.35×10^{-9}**	**this work**
S2+PdO (Al_2O_3=6 nm)	**800**	**176 fs**	**$+3.01\times10^{-10}$**	**1.1×10^{-5}**	**2.52×10^{-8}**	**this work**
S3+PdO (Al_2O_3=12 nm)	**800**	**176 fs**	**$+5.31\times10^{-11}$**	**0.5×10^{-5}**	**4.57×10^{-9}**	**this work**
S2+PdO (Al_2O_3=6 nm)	**400**	**176 fs**	**15×10^{-11} (at I_0 = 9.43 GW/cm^2)**	**3.0×10^{-6}**	**18.32×10^{-9}**	**this work**
S3+PdO (Al_2O_3=12 nm)	**400**	**176 fs**	**6.9×10^{-11} (max)**	**1.0×10^{-6} (min)**	**8.41×10^{-9}**	**this work**

The nonlinear quality factor $W = |n_2|/(\beta\lambda)$ [4] takes on opposite values for different configurations and wavelengths under study, reflecting the diversity of nonlinear modes available within this single architecture of the material. At a wavelength of 800 nm, S3+PdO exhibits a value of $W>>1$ due to a small β combined with a large positive value of $n_2 = +5.31\times10^{-11}$ cm^2/W, which results from the sign change induced by the PdO layer. This makes S3+PdO the most promising configuration for all-optical switching and nonlinear phase modulation at near-infrared wavelengths with femtosecond laser pulse durations. At a wavelength of 400 nm, the value of W for S2+PdO is limited by the dominant $Im\chi^{(3)}$, which corresponds to the absorptive nature of the optical nonlinearity of this nearly resonant configuration. Taken together, these contrasting performance metrics demonstrate that nanometer-scale tuning of the thickness of the Al_2O_3 barrier and the top PdO layer provides independent control over the sign, magnitude, and $Re\chi^{(3)}/Im\chi^{(3)}$ ratio. This enables the design of heterostructures optimized for various application contexts: nonlinear phase elements (S3+PdO at 800 nm), optical limiters and saturable absorbers (S1+PdO, S2+PdO at 800 nm), and nonlinear absorbers with resonant amplification (S2+PdO at 400 nm). Thus, the results obtained confirm that controlling the thickness of the Al_2O_3 barrier is an effective design principle for simultaneously controlling the sign, magnitude, and mechanism of nonlinear absorption in a single plasmonic heterostructure.

4. Conclusions

Investigations using femtosecond Z-scan spectroscopy (λ = 800 and 400 nm, τ_p = 176 fs) of nanocomposite heterostructures Ag/AuNP-Al_2O_3-PdO with an Al_2O_3 insulating layer thickness ranging from 1.5 to 12 nm revealed that the design of barriers on the nanometer scale enables simultaneous and independent control over the sign, magnitude, and *Re/Im* ratio of the third-order complex nonlinear optical susceptibility $\chi^{(3)}$ within a single plasmonic architecture.

At λ = 800 nm, the deposited PdO layer causes a change in the sign of n_2 in the S3+PdO sample with a thick barrier (d(Al_2O_3) = 12 nm), from -0.81×10^{-11} to $+5.31\times10^{-11}$ cm^2/W. This is explained by the dominance of the positive contribution from bound PdO electrons in the subband over the negative in-band Kerr term of the Ag/Au nanoparticles, when hot carrier tunneling is suppressed by the thick Al_2O_3 barrier. In sample S2+PdO with an intermediate barrier (d(Al_2O_3) = 6 nm), the deposition of PdO leads to an increase in $|\chi^{(3)}|$ by approximately 1625 times, reaching 2.52×10^{-8} esu. This is the highest value recorded for Ag/Au nanoparticle films excited by a femtosecond pulse at this wavelength, which is due to the enhancement of the cross-section of PdO's nonlinear absorption in the near field by plasmons. In both cases, at high magnifications of $|\chi^{(3)}|$, $Im\chi^{(3)}$ dominates rather than $Re\chi^{(3)}$, indicating that the contribution of PdO to optical nonlinearity is of an absorptive rather than a refractive nature.

At λ = 400 nm, the deposition of PdO leads to a change in the non-linear absorption mechanism from predominantly RSA to predominantly SA across the entire series of samples. In this case, β decreases by one or two orders of magnitude. All three configurations exhibit qualitatively different dependencies on laser intensity, which are determined by barrier-controlled hot carrier transport. In S1+PdO (d(Al_2O_3) = 1.5 nm), n_2 and β decrease monotonically. In S2+PdO (d(Al_2O_3) = 6 nm), a threshold jump in I_s occurs with a correlated minimum in β at $I_0 \sim 15$ GW/cm^2, which is explained by the sequential saturation of interphase trap states and the bulk PdO. In S3+PdO (d(Al_2O_3) = 12 nm), a non-monotonic behavior of the Kramer's-Kronig-related dependencies $n_2(I_0)$ and $\beta(I_0)$ is observed, arising from the blocking of hot carrier transition across a thick barrier. At 400 nm, the maximum $|\chi^{(3)}|$, which is 18.32×10^{-9} esu for S2+PdO, exceeds by more than an order of magnitude the value determined for the corresponding configuration without a PdO coating.

The non-linear quality factor $W = |n_2|/(\beta\lambda)$ highlights the potential for applying various configurations. For instance, S3+PdO at 800 nm exhibits a value of $W >> 1$ and is a promising candidate for all-optical switching and nonlinear phase modulation at wavelengths in the near-infrared range under the action of femtosecond laser pulses, whilst S2+PdO at 400 nm is optimized for applications involving resonance-enhanced nonlinear absorption. These results confirm that the thickness of the Al_2O_3 is a key structural parameter for controlling the third-order nonlinear optical response of Ag/AuNP-Al_2O_3-PdO plasmonic heterostructures, opening up prospects for the development of tunable optical limiters, saturating absorbers and all-optical switches based on a single material platform.

References

1. Hache F, Ricard D, Flytzanis C (1986) Optical nonlinearities of small metal particles: surface-mediated resonance and quantum size effects. J Opt Soc Am B 3:1647–1655. https://doi.org/10.1364/JOSAB.3.001647

2. Flytzanis C, Hache F, Klein MC, Ricard D, Roussignol P (1991) Nonlinear optics in composite materials: 1. Semiconductor and metal crystallites in dielectrics. In: Wolf E (ed) Progress in Optics, vol 29. Elsevier, Amsterdam, pp 321–411. https://doi.org/10.1016/S0079-6638(08)70009-X

3. Sheik-Bahae M, Said AA, Wei TH, Hagan DJ, Van Stryland EW (1990) Sensitive measurement of optical nonlinearities using a single beam. IEEE J Quantum Electron 26:760–769. https://doi.org/10.1109/3.53394

4. Zhang YX, Wang YH (2017) Nonlinear optical properties of metal nanoparticles: a review. RSC Adv 7:45129–45144. https://doi.org/10.1039/C7RA07551K

5. Johnson PB, Christy RW (1972) Optical constants of the noble metals. Phys Rev B 6:4370–4379. https://doi.org/10.1103/PhysRevB.6.4370

6. Hache F, Ricard D, Flytzanis C, Kreibig U (1988) The optical Kerr effect in small metal particles and metal colloids: the case of gold. Appl Phys A 47:347–357. https://doi.org/10.1007/BF00615498

7. Borshch AA, Brodin MS, Volkov VI, et al (2006) Giant nonlinear refraction in gold island films. JETP Lett 84:214–216. https://doi.org/10.1134/S0021364006160107

8. Tomchuk PM, Brodyn MS, Volkov VI, Lyakhovetskyi VR (2013) Third-order optical nonlinearity of noble metal nanostructures. Ukr J Phys Rev 8:1. http://archive.ujp.bitp.kiev.ua/files/reviews/8/1/r08_01_03.pdf

9. Rudenko V, Styopkin V, Liakhovetskyi V, Brodin A (2026) Tunable third-order optical nonlinearity in Ag/Au nanostructures with Al_2O_3 coating layer under femtosecond and nanosecond excitation. Appl Nanosci 16:3. https://doi.org/10.1007/s13204-025-03138-2

10. Nilchi A, Dehaghan M, Maalek S, Maalek B (2015) Band gap engineering of PdO thin films: optical properties. J Mater Sci Mater Electron 26:4937–4943. https://doi.org/10.1007/s10854-015-2991-9

11. Sheik-Bahae M, Hutchings DC, Hagan DJ, Van Stryland EW (1991) Dispersion of bound electronic nonlinear refraction in solids. IEEE J Quantum Electron 27:1296–1309. https://doi.org/10.1109/3.89946

12. Brodyn MS, Volkov VI, Rudenko VI, Liakhovetskyi VR, Borshch AO (2017) Large third-order optical nonlinearity in PdO thin films. J Nonlinear Opt Phys Mater 26:1750037. https://doi.org/10.1142/S0218863517500370

13. Styopkin V, Rudenko V, Brodyn M, et al (2022) Characteristics of plasmon resonance of gold nanoparticles in three-layer systems AuNP-Al_2O_3-PdO(Pd). Plasmonics 17:859–867. https://doi.org/10.1007/s11468-021-01574-8

14. Rudenko V, Brodyn M, Liakhovetskyi V, Styopkin V (2023) Optical cubic nonlinearity of thin two-layer AuNP-Al_2O_3 and three-layer AuNP-Al_2O_3-PdO systems under nanosecond 1064 nm and 532 nm excitation. Opt Quantum Electron 55:420. https://doi.org/10.1007/s11082-023-04698-9

15. Simmons J (1963) Generalized formula for the electric tunnel effect between similar electrodes separated by a thin insulating film. J Appl Phys 34:1793–1803. https://doi.org/10.1063/1.1702682

16. Venkatram N, Rao DN, Akundi MA (2005) Nonlinear absorption, scattering, and optical limiting studies of CdS nanoparticles. Opt Express 13:867–872. https://doi.org/10.1364/OPEX.13.000867

17. Zhao J, Ruan Q, Tang R, Zhu J, Zeng H, Wang J (2021) Plasmonic saturable absorbers. Adv Photonics Res 2:2100003. https://doi.org/10.1002/adpr.202100003

18. Kwak CH, Lee YL, Kim SG (1999) Analysis of asymmetric Z-scan measurement for large optical nonlinearities in an amorphous As_2S_3 thin film. J Opt Soc Am B 16:600–604. https://doi.org/10.1364/JOSAB.16.000600

19. Zhang F, Wang Z, Wang D, Wu Z, Wang S, Xu X (2016) Nonlinear optical effects in nitrogen-doped graphene. RSC Adv 6:3526–3531. https://doi.org/10.1039/C5RA22715B

20. Harutyunyan H, Martinson A, Rosenmann D, Khorashad LK, Besteiro LV, Govorov AO, Wiederrecht GP (2015) Anomalous ultrafast dynamics of hot plasmonic electrons in nanostructures with hot spots. Nat Nanotechnol 10:770–774. https://doi.org/10.1038/nnano.2015.165

21. Sun X, Xiong Y, Chen P, et al (2000) Investigation of an optical limiting mechanism in gold nanoparticles. Appl Opt 39:1998–2001. https://doi.org/10.1364/AO.39.001998

22. Abd El-Salam Y, Adday HD, Abdel Samad F, Qayyum H, Mohamed T (2024) Using femtosecond laser pulses to explore the nonlinear optical properties of Ag/Au alloy nanoparticles synthesized by pulsed laser ablation in a liquid. Nanomaterials 14:1290. https://doi.org/10.3390/nano14151290

23. Santos JCC, Vencato CA, Sigoli FA, Mazali IO, Brito-Silva AM (2021) Nonresonant nonlinear optical switching behavior of Ag monometallic and Ag@Au bimetallic investigated by femtosecond Z-scan measurements. Opt Laser Technol 143:107335. https://doi.org/10.1016/j.optlastec.2021.107335

24. Liu X, Wang Q, Zhang Y, Li H, Xue M (2022) Synthesis, characterization, and femtosecond third-order optical nonlinearity of Au@Ag core-shell nanoparticles. J Nonlinear Opt Phys Mater 31:2250002. https://doi.org/10.1142/S0218863522500023

25. Sreenivasulu G, Babu KV, Prasad G, Rao BA, Veeraiah N (2020) Investigations on nonlinear optical properties of gold nanoparticles doped fluoroborate glasses for optical limiting applications. J Non-Cryst Solids 534:119938. https://doi.org/10.1016/j.jnoncrysol.2020.119938

26. Alesenkov A, Pilipavičius J, Beganskienė A, Sirutkaitis R, Sirutkaitis V (2015) Nonlinear properties of silver nanoparticles explored by a femtosecond Z-scan technique. Lith J Phys 55:100–109. https://doi.org/10.3952/physics.v55i2.3100

27. Kaniyarakkal S, Thomas T, Sadagopalan SK, Jayamohan L, Muralimanohar R, Vasanthakumaryamma L, Nair VS (2022) Synthesis, linear and nonlinear optical properties of Ag/Al_2O_3 nanocomposites. Materials 15:6322. https://doi.org/10.3390/ma15186322

Declarations

Funding: *This work was performed within project B-189 of the target complex program of basic research of the NAS of Ukraine.*

Conflicts of interest/Competing interests: *The authors have no relevant financial or non-financial interests to disclose.*

Availability of data and material: the datasets generated during and/or analyzed during the current study are available from the corresponding author upon reasonable request.

Code availability: Not applicable.

Author Contributions Statement

V.I. Rudenko wrote the main manuscript text.

V.I. Styopkin prepared the samples and participated in the discussion of the results of the experiments.

V.R. Liakhovetskyi prepared figures and participated in the discussion of the results of the experiments.

All authors reviewed the manuscript.

Ethics approval: Not applicable

Consent to participate: Not applicable

Consent for publication: Not applicable